JOURNAL OF PROPULSION AND POWER
Vol. 27, No. 3, May–June 2011

Numerical Prediction of Conjugate Heat Transfer in Fluid Network

Alok Majumdar*
NASA Marshall Space Flight Center, Huntsville, Alabama 35812
and
S. S. Ravindran†
University of Alabama in Huntsville, Huntsville, Alabama 35899

DOI: 10.2514/1.B34037

An unsteady finite volume procedure for conjugate heat transfer in a flow network is presented that takes into account the longitudinal conduction through the solid. It uses a fully coupled approach in which the governing equations for solid and fluid are coupled through solid-to-fluid heat transfer that is expressed as a function of flow properties and temperature of the solid. As an evaluation of the proposed technique, a chilldown problem for a cryogenic transfer line is formulated and solved. Test cases modeling transient flow of liquid hydrogen and liquid nitrogen under saturated and subcooled liquid conditions are presented. The effects of varying the inlet driving pressure on the chilldown time and flow rates have been evaluated. Increasing the driving pressure decreases the chilldown time and increases the flow rate. Subcooling the inlet cryogen further reduces the chilldown time. Numerical predictions are compared with available experimental data and are found to be in good agreement. The proposed model captures the essential features of conjugate heat transfer and provides an efficient and robust way for predicting chilldown of transfer line at a low computational cost.

Nomenclature

A	=	cross-sectional area, ft^2
A_{cc}	=	tube cross-sectional area, ft^2
a	=	speed of sound, ft/s
C_f	=	specific heat of the fluid, Btu/lb°F
C_L	=	flow coefficient
C_p	=	specific heat at constant pressure, Btu/lb°F
c	=	wave speed, ft/s
D	=	diameter of the pipe, ft
f^*	=	Darcy–Weisbach friction factor
g_c	=	gravitational constant, 32.174 lb-ft/lbf · s^2
h	=	enthalpy, Btu/lb
h_c	=	heat transfer coefficient, Btu/(ft-s°F)
J	=	mechanical equivalent of heat, 778 ft-lbf/Btu
K_{f^*}	=	flow resistance coefficient, lbf-s^2/(lb-ft)^2
K_{rot}	=	nondimensional rotating flow resistance coefficient
k	=	thermal conductivity, Btu/(ft-s°F)
L	=	length of the tube, ft
$\dot{m}$	=	mass flow rate, lb/s
m	=	resident mass, lb
Nu	=	Nusselt number
Pr	=	Prandtl number
Re	=	Reynolds number
n	=	number of branches
p	=	pressure, lbf/ft^2
$\dot{Q}$	=	heat source, Btu/s
$\dot{q}$	=	heat transfer rate, Btu/s
R	=	gas constant, lbf-ft/lb-R
r	=	radius, ft
$\dot{S}$	=	heat source, Btu/s
S	=	momentum source, lb
T	=	temperature, °F
t	=	time, s
V	=	volume, ft^3
v	=	fluid velocity, ft/s
z	=	compressibility factor
δ	=	tube-wall characteristic length, ft
ε	=	surface roughness of pipe, ft
ρ	=	density, lb/ft^3
ϕ	=	specific volume, specific heat, or viscosity

Subscripts

f	=	liquid state
g	=	vapor state
i	=	ith node
ij	=	branch connecting nodes i and j
j	=	jth node
s	=	solid node
sa	=	solid to ambient
sf	=	solid to fluid
ss	=	solid to solid
u	=	upstream

Received 3 June 2010; revision received 19 September 2010; accepted for publication 24 September 2010.

*Aerospace Technologist, Thermal and Combustion Analysis Branch. Member AIAA.
†Associate Professor, Department of Mathematical Sciences.

I. Introduction

THE conjugate heat transfer problem is a coupled fluid–structure heat transfer problem in which conduction heat transfer in a solid wall interacts with fluid flow and the convection heat transfer in fluid flow interacts at the solid boundary. Fluid network modeling with conjugate heat transfer has many applications in aerospace engineering and others. In modeling unsteady flow with heat transfer, it is important to know the variation of wall temperature in time and space to be able to calculate heat transfer from solid to fluid. Since wall temperature is a function of flow, a coupled analysis of temperature of solid and fluid is necessary.

In cryogenic applications, such as medical and space technology, modeling of conjugate heat transfer is of great importance. In space technology applications, correct prediction of boil-off rate in propellant tanks and chilldown of transfer lines are of great engineering value. The operation of a cryogenic propulsion system, such as those found in spacecraft and missiles, requires transfer-line chilldown before establishing a steady flow of cryogenic fluid between various system components. The primary objective is to cool the line (Fig. 1) as fast as possible so as to attain homogeneous liquid transfer. When liquid cryogen at saturation temperature begins to flow in a tube, initially at ambient temperature, the liquid instantly vaporizes near

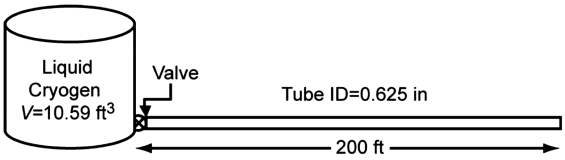

Fig. 1 Schematic of cryogenic line chilldown experimental setup.

the tube wall. Therefore, a cross section of the flow will have an outer vapor ring with a saturated liquid core. As the flow moves downstream, the liquid core evaporates, and the vapor becomes superheated. As the tube wall cools, the liquid core penetrates farther and beyond downstream. Eventually, the tube becomes filled with liquid. Because of change in fluid density, the average velocities are significantly higher in the vapor region of the tube. Prediction of chilldown time requires modeling of these transient phenomena and understanding of how they affect heat transfer from the tube wall to the flowing cryogen.

Several experimental and computational studies of the chilldown of various types of transfer lines have been reported in the literature [1–12]. In [4], chilldown of an LN_2 flow in a vertical tube was experimentally investigated. Experimental studies into the chilldown of a horizontal tube by an LN_2 flow with low mass flow rates were presented in [11]. In [10], experimental investigations into the heat transfer characteristics and flow regimes of nitrogen and hydrogen were presented. In [6], an analytical model of the chilldown was presented under the assumption of constant flow rate, heat transfer coefficient, and fluid properties. In [7], a numerical modeling of a one-dimensional chilldown process was presented using a finite difference method. In [5], a finite-volume-based numerical modeling was presented for prediction of the chilldown of a cryogenic transfer line, based only on transient heat transfer effects and neglecting fluid transient effects. Subsequently, it was extended to include fluid transient effects in [8]. Conjugate heat transfer analysis presented in [5,8] modeled the solid nodes in an ad hoc manner in which conservation equations for solid were solved at the beginning of each time step, and solid temperatures were used to calculate heat transfer to the fluid node. Although successful comparison of numerical solution with analytical solution for a short tube was reported in [5], the results presented in [8] for a long tube did not match the experimental data well. The mismatch is partly due to the semicoupled fluid–solid-heat transfer modeling and partly due to the fact that longitudinal conduction between solid nodes was not accounted for in their model.

The purpose of this paper is to present a fully coupled fluid–solid network modeling for conjugate heat transfer problems. In network modeling, the conservation equations are first expressed in finite volume form for a network. Flow domain is discretized into a series of discrete nodes connected by branches. Each internal node is connected to other solid nodes and the solid nodes are in turn connected to other solid nodes via conductors (see Fig. 2). In this framework, conservation equations for both solid and fluids are solved simultaneously using an unsteady network finite volume approach. The mass and energy conservation equations are solved at the nodes, whereas momentum conservation equations are solved at the branches. The energy conservation equations for solid nodes are solved to determine the temperatures of the solid nodes simultaneously with all conservation equations governing fluid flow. However, the simultaneous nonlinear system that arises in network flow modeling with conjugate heat transfer can be prohibitively large. Therefore, current implementation of some fast algorithms for solving the fully discrete system of nonlinear conservation equations is presented. The numerical algorithms described in this paper was implemented in a general-purpose computer program, Generalized Fluid System Simulation Program [13] and was used to carry out the numerical experiments.

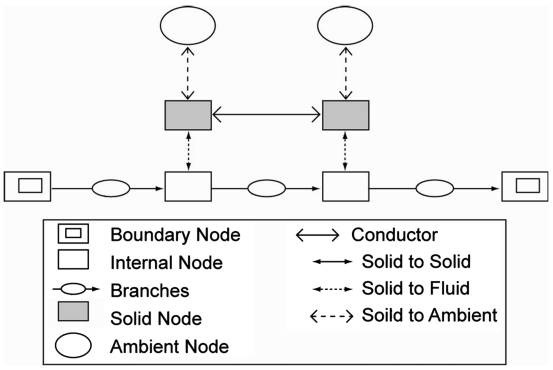

Fig. 2 Flow network consisting of fluid nodes, solid nodes, flow branches, and conductors.

The feasibility of the proposed network conjugate heat transfer approach is shown in predicting the chilldown in a long cryogenic transfer line. Two chilldown cases using LH_2 and LN_2 as the working fluid are studied. Numerical predictions by the proposed approach are validated by comparing the results with the experimental investigations reported in [9]. This experiment was initiated to characterize the thermal response of the transfer line using LH_2 and LN_2 as the fluids for several different conditions. The experimental setup consisted of a 10.59-ft^3 (300 liter) supply tank; an inlet valve; and a 200-ft-long (60.96-m-long), 0.75-in.-o.d. by 0.625-in.-i.d. (1.59-cm-i.d.) vacuum-jacketed copper transfer line that exhausted to atmosphere. Three different inlet valves [a 0.75-in.-port (1.91-cm-port) ball valve, a 1-in.-port (2.54-m-port) globe valve, and a 1-in.-port (2.54-cm-port) gate valve] were used in the National Bureau of Standards experiments. The exit end of the pipe was open to the atmosphere, which was 0.82 atm in Boulder, Colorado.

The unsteady network finite volume approach for conjugate heat transfer is presented in Sec. II. Computational results and discussion are given in Sec. III. Section IV presents some conclusions drawn from the study.

II. Finite Volume Formulation of Fluid Network

A. Governing Equations

Numerical modeling of the conjugate heat transfer process in a cryogenic transfer line requires a solution of unsteady mass, momentum, and energy conservation equations in conjunction with thermodynamic equations of state. The finite volume formulation requires that governing equations be written in a conservative form for a flow network involving boundary nodes, internal nodes, and branches (see Fig. 2). The flow domain is divided into a discrete number of control volumes and the conservation equations of mass, momentum, and energy are determined for each control volume. At boundary nodes, pressures and temperatures are prescribed. At internal nodes, pressures and temperatures are computed by solving time-dependent mass and energy conservation equations. Each internal node is a control volume where there are inflow and outflow of mass and energy at the boundaries of the control volume. Figure 1 shows a long pipeline connected to a tank with a valve placed at the beginning of the pipeline. Flow in a pipe may be considered as a series of discrete fluid nodes connected by branches. One boundary node represents the tank, and the other boundary node represents the ambient where the fluid is discharged.

The discretization scheme assumes that the flow is driven by the pressure differential between the upstream and downstream nodes. This is known as the staggered grid technique that is extensively used in solving Navier–Stokes equations by the finite volume method [14]. Mass and energy conservation equations are solved at the internal nodes in conjunction with thermodynamic equation of state. Flow rates are computed at the branches by solving the time-dependent momentum conservation equation. This process of discretization allows the development of the set of conservation equations in an unstructured coordinate system. Figure 2 displays a schematic showing adjacent nodes, their connecting branches, and the indexing system used by the network solver.

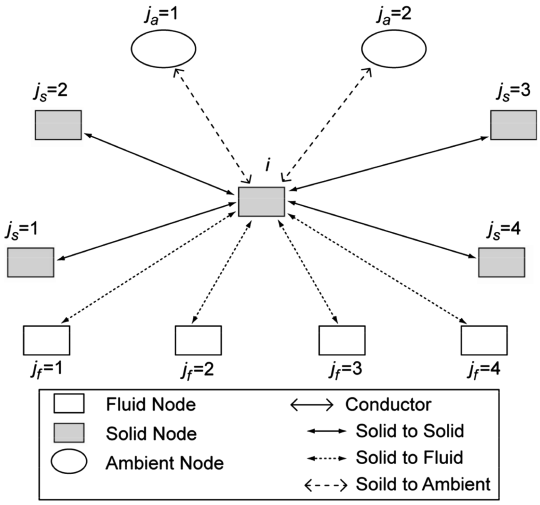

Fig. 3 Schematic showing the connection of a solid node with neighboring solid, fluid, and ambient nodes.

1. Mass Conservation Equation

The mass conservation equation at the ith node can be expressed as

$$\frac{(m_i)_{t+\Delta t} - (m_i)_t}{\Delta t} = -\sum_{j=1}^{n} \dot{m}_{ij} \tag{1}$$

Equation (1) requires that, for the transient formulation, the net mass flow from a given node must equate to the rate of change of mass in the control volume.

2. Energy Conservation

The energy conservation equation for node i, shown in Fig. 3, can be expressed following the first law of thermodynamics and using enthalpy as the dependent variable. It can be written as

$$\frac{m(h - \frac{p}{\rho J})_{t+\Delta t} - m(h - \frac{p}{\rho J})_t}{\Delta t} = \sum_{j=1}^{n} \{\max[-\dot{m}_{ij}, 0]h_j - \max[\dot{m}_{ij}, 0]h_i\} + \dot{Q}_i \tag{2}$$

Equation (2) shows that for transient flow, the rate of increase of internal energy in the control volume is equal to the rate of energy transport into the control volume minus the rate of energy transport from the control volume plus any external rate of heat transfer from the solid node ($\dot{q}_{sf}$). The maximum operator used in Eq. (2) is known as an upwind differencing scheme and has been extensively employed in the numerical solution of Navier–Stokes equations in convective heat transfer and fluid flow applications [14]. When the flow direction is not known, this operator allows the transport of energy only from its upstream neighbor. In other words, the upstream neighbor influences its downstream neighbor but not vice versa.

3. Momentum Conservation Equation

The flow rate in a branch is calculated from the momentum conservation equation, which represents the balance of fluid forces acting on a given branch (see Fig. 2). Inertia, pressure, and friction are considered in the conservation equation. Also note that the flow rate $\dot{m}_{ij}$, is a vector quantity. A negative value of $\dot{m}_{ij}$ signifies that the flow is directed from the jth node to the ith node:

$$\frac{(mu)_{t+\Delta t} - (mu)_t}{g_c \Delta t} + \max[\dot{m}_{ij}, 0](u_{ij} - u_u) - \max[-\dot{m}_{ij}, 0](u_{ij} - u_u) = (p_i - p_j)A_{ij} - K_{f^*}\dot{m}_{ij}|\dot{m}_{ij}|A_{ij} \tag{3}$$

The two terms on the left side of the momentum equation represent the inertia of the fluid. The first term is the time dependent term that must be considered for unsteady calculations. The second term is significant when there is a large change in area or density from branch to branch. The first term on the right side of the momentum equation represents the pressure gradient in the branch. The second term represents the frictional effect. Friction is modeled as a product of K_{f^*}, the square of the flow rate, and area. K_{f^*} is a function of the fluid density in the branch and the nature of flow passage being modeled by the branch. For a pipe with length L and diameter D, K_{f^*} can be expressed as

$$K_{f^*} = \frac{8f^*L}{\rho_u \pi^2 D^5 g_c}$$

The Darcy–Weisbach friction factor f^* in the definition of K_{f^*} is calculated from the Colebrook equation [15], which is expressed as

$$\frac{1}{f^*} = -2\log\left[\frac{\varepsilon}{3.7D} + \frac{2.51}{Re\sqrt{f^*}}\right]$$

where ε/D is the surface roughness factor and Re is the Reynolds number. The density and viscosity for the Reynolds number are computed from quality, assuming homogeneous mixture, to account for two-phase flow. The momentum conservation equation also requires knowledge of the density and the viscosity of the fluid within the branch. These are functions of the temperatures and pressures and can be computed using the thermodynamic property program in [16] that provides the thermodynamic and transport properties for different fluids.

4. Equation of State

Transient flow calculations require the knowledge of resident mass in a control volume. The resident mass in the ith control volume is calculated from the equation of state for real fluids:

$$m = \frac{pV}{RTz} \tag{4}$$

The compressibility factor z and temperature T in Eq. (4) are calculated from the thermodynamic property program [16] for a given pressure and enthalpy. The pressure, enthalpy, and resident mass in internal nodes and the flow rate in branches are calculated by solving the fully coupled nonlinear system of Eqs. (1–4), respectively. There is no explicit equation for pressure. The pressure is calculated implicitly from the mass conservation equation.

5. Phase Change

Modeling phase change is fairly straightforward in the present formulation. The vapor quality of the saturated liquid–vapor mixture is calculated from

$$x = \frac{h - h_f}{h_g - h_f}$$

Assuming a homogeneous mixture of liquid and vapor, the density, specific heat, and viscosity are computed from the following relations:

$$\phi = (1 - x)\phi_f + x\phi_g$$

where φ represents specific volume, specific heat, or viscosity.

6. Energy Conservation Equation for Solid Node i

In fluid–solid network for conjugate heat transfer, solid nodes, ambient nodes, and conductors become part of the flow network. A typical flow network for conjugate heat transfer is shown in Fig. 3. The energy conservation equation for the solid node is solved in conjunction with all other conservation equations. The energy conservation for solid node i can be expressed as

$$\frac{(mC_pT_s^i)_{t+\Delta t} - (mC_pT_s^i)_t}{\Delta t} = \sum_{j_s=1}^{n_{ss}} \dot{q}_{ss} + \sum_{j_f=1}^{n_{sf}} \dot{q}_{sf} + \sum_{j_a=1}^{n_{sa}} \dot{q}_{sa} + \dot{S}_i \tag{5}$$

The left-hand side of the equation represents rate of change of temperature of the solid node i. The right-hand side of the equation represents the heat transfer from the neighboring node and heat source or sink. The heat transfer from neighboring solid, fluid, and ambient nodes can be expressed as follows:

$$\dot{q}_{ss} = k_{ij_s}A_{ij_s}/\delta_{ij_s}(T_s^{j_s} - T_s^i) \tag{6a}$$

$$\dot{q}_{sf} = h_{ij_f}A_{ij_s}(T_f^{j_f} - T_s^i) \tag{6b}$$

and

$$\dot{q}_{sa} = h_{ij_a}A_{ij_a}(T_a^{j_a} - T_s^i) \tag{6c}$$

The heat transfer rate can be expressed as a product of conductance and temperature differential. The conductance for Eqs. (6a–6c) is

$$C_{ij_s} = \frac{k_{ij_s}A_{ij_s}}{\delta_{ij_s}}; \qquad \mathrm{C}_{ij_f} = h_{ij_f}A_{ij_f}; \qquad \mathrm{C}_{ij_a} = h_{ij_a}A_{ij_a} \tag{7}$$

where effective heat transfer coefficients for solid-to-fluid and solid-to-ambient nodes are expressed as

$$h_{ij_a} = h_{c,ij_a} + h_{r,ij_a}$$

$$h_{r,ij_f} = \frac{\sigma[(T_f^{j_f})^2 + (T_s^i)^2][T_f^{j_f} + T_s^i]}{\frac{1}{\varepsilon_{ij,f}} + \frac{1}{\varepsilon_{ij,s}} - 1}$$

and

$$h_{r,ij_a} = \frac{\sigma[(T_f^{j_a})^2 + (T_s^i)^2][T_a^{j_a} + T_s^i]}{\frac{1}{\varepsilon_{ij,a}} + \frac{1}{\varepsilon_{ij,s}} - 1}$$

For the heat transfer coefficient specification we will neglect nucleate boiling and employ the modified Miropolski's correlation [17] for two-phase flow:

$$Nu = h_cD/k_v$$

where

$$Nu = 0.023(Re_{\mathrm{mix}})^{0.8}(Pr)^{0.4}(Y)$$

where

$$Re_{\mathrm{mix}} = \left(\frac{\rho uD}{\mu_g}\right)\left[x + \left(\frac{\rho_g}{\rho_1}\right)(1-x)\right],$$

$$Pr_g = \left(\frac{C_p\mu_g}{k_g}\right), \quad \text{and} \quad Y = 1 - 0.1\left(\frac{\rho_g}{\rho_1} - 1\right)^{0.4}(1-x)^{0.4}$$

The neglect of nucleate boiling in cryogenic flows with large initial wall superheat (difference in temperature between the duct wall and the fluid at saturation) is expected to have only a minor effect on the overall chilldown. The reason for this is that film boiling remains down to a relatively low superheat after most of the cooling has occurred. As a result, the amount of heat transfer occurring during nucleate boiling is relatively small when compared with the total heat transfer given the initial temperature difference between the fluid and structure. Furthermore, since heat flux increases as peak heat flux is approached from minimum heat flux in film boiling, the boiling curve passes through the nucleate boiling regime very quickly.

It may be also noted that radiative heat transfer and heat transfer to ambient have not been included in the computations presented in this paper because of their negligible effect on chilldown of vacuum-jacketed copper transfer lines.

B. Nonlinear Discrete System Solvers

Conjugate heat transfer in network modeling presents a unique coupling among the governing equations: namely, the coupling among mass conservation, momentum conservation, and equation of state is stronger than other equations such as the enthalpy equation or energy equation for solids. The lack of strong coupling among equations is exploited to devise a divide-and-conquer strategy, whereby the equations that are more strongly coupled are solved in one set of equations and the equations that are not strongly coupled are solved in the other set of equations. This strategy, as demonstrated in the sequel, leads to significant memory and computational time savings. The continuity and momentum equations are rewritten such that the pressures and flow rates can be estimated at each node. Traditional network solvers [18,19] use a combination of the successive substitution (SS) method and Newton's method to solve the nonlinear systems. Newton's method for solving the nonlinear algebraic system is computationally costly for large-scale flow network problems involving a large number of nodes and branches. The major part of the computational complexity comes from the computation and inversion of the Jacobian matrix. Broyden's method was therefore employed for solving the discrete nonlinear system. In Broyden's method [2,20], one replaces the inverse Jacobian matrix with a suitable approximate inverse Jacobian matrix and updates it as iteration progresses. For solving a discrete nonlinear system $F(x) = 0$, the Broyden method can be stated as follows:

Compute

$$\Delta x^k = -B_k^{-1}F(x^k)$$

and update the solution as

$$x^{k+1} = x^k + \Delta x^k$$

where B^{-1} is the approximation to the inverse Jacobian matrix.

Broyden's method is fast and suitable for computing transient problems and problems that require computation in a long time interval (see [2] for more details). The inverse update procedure has the advantage of not having to use Gaussian elimination to solve the linear algebraic system. An added advantage of this divide-and-conquer strategy over the all-at-once fully simultaneous strategy is that the fixed-point iterate can be used as the initial guess for Newton's method, thus improving the convergence characteristics of Newton's method and the overall algorithm. In Sec. III, four solvers will be implemented on a test problem involving conjugate heat transfer in a cryogenic pipeline: namely, Newton, Newton-SS, Broyden, and Broyden-SS. In the Newton solver, all the conservation equations are solved by Newton's method. In the Newton-SS solver, the tightly coupled continuity equation, momentum equation, and equation of state are solved by Newton's method and the energy equation is solved by the successive substitution method. In the Broyden solver, all the conservation equations are solved by Newton's method, and in the Newton-SS, tightly coupled continuity equation, momentum equation, and equation of of state are solved by Newton's method. The energy equation is solved by the successive substitution method.

III. Results and Discussion

The verification and validation of the finite volume procedure for the prediction of conjugate heat transfer in a fluid network was performed by comparing the predictions with available experimental results for a long cryogenic transfer-line model reported in [9]. Figure 1 shows a schematic of the experimental setup, which consists of a 200-ft-long, 0.625-in.-i.d. copper tube supplied by a 300 liter tank through a valve and exits to the atmosphere ($\approx$12.05 psia). The tank was filled with either LH_2 or LN_2. At time zero, the valve at the left end of the pipe was opened, allowing liquid from the tank to flow into the ambient pipeline driven by tank pressure.

Before applying the proposed conjugate heat transfer approach and the computer code to solve a real cryogenic chilldown problem, they were validated first by simulating a conduction–convection heat transfer in a circular rod between two walls. It was then used to simulate a simple chilldown process in an LH_2 transfer line for a driving pressure for which analytical solutions are available. Numerical predictions were compared with known analytical solutions [2]. Validation results showed excellent agreement, proving that the computer code is reliable. The model and computer code were then used to simulate the cryogenic chilldown process described in [9]. The numerical model consisted of a 200-ft-long, 0.625-in.-i.d. copper tube. The initial tube temperature in the experimental measurements [9] varied slightly, due to variations in ambient temperature. As these data were not reported in numerical form in [9], they were digitally extracted from their plots and used in the computational model as initial transfer-line temperatures. Pressure at the outlet was set at 12.05 psia.

Figure 4 shows a schematic of the network flow model that was constructed to simulate the transfer line. The tube was discretized into 33 fluid nodes (two boundary nodes and 31 internal nodes), 31 solid nodes, and 32 branch nodes. The upstream boundary node represents the cryogenic tank, and the downstream boundary node represents the ambient, where the fluid is discharged. The first branch represents the valve; the next 30 branches represent the transfer line. Each internal node is connected to a solid node (nodes 34 through 64) by a solid-to-fluid conductor. At the internal fluid nodes and branches, mass, momentum, and energy equations are solved in conjunction with the thermodynamic equation of state to compute the pressures, flow rates, temperatures, densities, and other thermodynamic and thermophysical properties. The heat transfer in the wall is modeled using the lumped-parameter method, assuming the wall radial temperature gradient is small. At the internal solid nodes, the energy equation is solved in conjunction with all other conservation equations. The heat transfer coefficient of the energy equation for the solid node was computed from the Miropolski correlation [17]. The experimental work reported in [9] did not provide details concerning the flow characteristics for the valve used, nor did they give a history of the valve opening times that they used. An arbitrary 0.05 s transient opening of the valve was used while assuming a linear change in flow area.

In the experiments, two liquid conditions were considered; the fluid within the supply tank was either pressurized and allowed to come to approximate thermal equilibrium at that pressure (saturated) or quickly pressurized from saturation at atmosphere pressure (subcooled). Pressure and temperature were recorded at four downstream stations along the line. These stations are located at 20, 80,

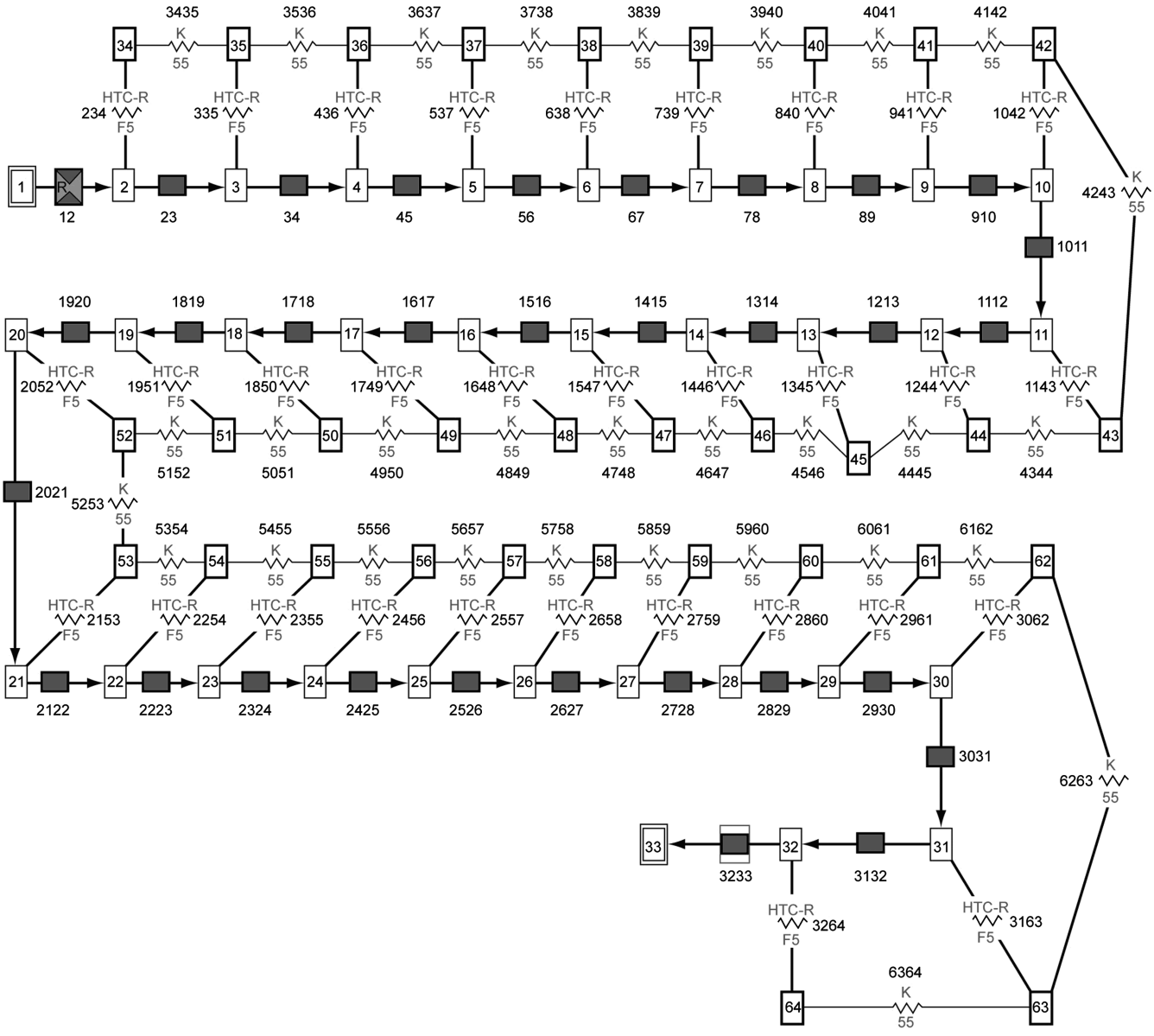

Fig. 4 Network flow model of the fluid system consisting of a tank, pipeline, and valve constructed with boundary nodes, internal nodes, and branches.

Table 1 Saturated LH_2 chilldown time for various driving pressures

Driving pressure, psia	Saturation temperature, °F	Experimental chilldown time, s	Predicted chilldown time, s
74.97	−411.06	68	70
86.73	−409.08	62	69
111.72	−406.4	42	50
161.72	−402.13	30	33

141, and 198 ft, respectively. In our numerical predictions, the chilldown of both hydrogen and nitrogen under saturated and subcooled conditions was investigated. In the network model, stations 1 through 4 are nodes in the model whose locations correspond to four measurement stations in the experiments [9]. All the simulations reported were performed with the model and consisted of a total of 31 solid nodes and 31 fluid nodes (internal) and the time step of $\Delta t = 0.0015$ s. Convergence was established when normalized residuals reduced to a value of 10^{-4}.

A. Chilldown of Hydrogen

For the subcooled LH_2 cases, propellant temperature in the tank was −424.57 °F and pressure was varied to get different levels of subcooling. Whereas for the saturated cases, the propellant temperature in the tank was the saturation temperature at the indicated driving pressure listed in Table 1. Figure 5 compares the wall temperature of the 33-node transfer line, grid-resolution predictions of the network model with the experimental transfer-line wall temperatures reported in [9] for four different inlet driving pressures. Stations 1 through 4 are nodes in the computational model whose locations correspond to four measurement stations in the original experimental setup. It can be seen by comparing the four cases in Fig. 5 that the 33-node network models' predictions agree well with the experimental results. A small discrepancy exists between prediction and experiments. This is partly due to coarseness of the network node, both solid and fluid, and partly due to the heat transfer coefficient that affects the longitudinal conduction that can be seen by noting that the discrepancy increases at each successive station in the downstream.

The predicted LH_2 chilldown time for various inlet driving pressures is presented in Fig. 6a. In this figure, comparison is made between prediction and experimental observation for the saturated and subcooled cases. Tables 1 and 2 give the numerical values for the driving pressures, inlet temperatures, and the corresponding chilldown times. Here, the chilldown time is defined as the time corresponding to the low-temperature knee for a given transfer-line wall-temperature curve. The network flow model prediction again compares well with experimental results even with a 33-node grid. A grid refinement study shown in Sec. III.B indicates that further grid refinement may not improve the accuracy significantly. As can be seen in Fig. 6a, the numerical model tends to slightly overpredict the cooldown times (see also Tables 1 and 2). Likely reasons for computational results not matching experimental results are 1) inaccuracy of Miropolski heat transfer correlation 2) representation of friction factor in two-phase flow assuming homogeneous mixture, and 3) uncertainty in the experimental data being compared.

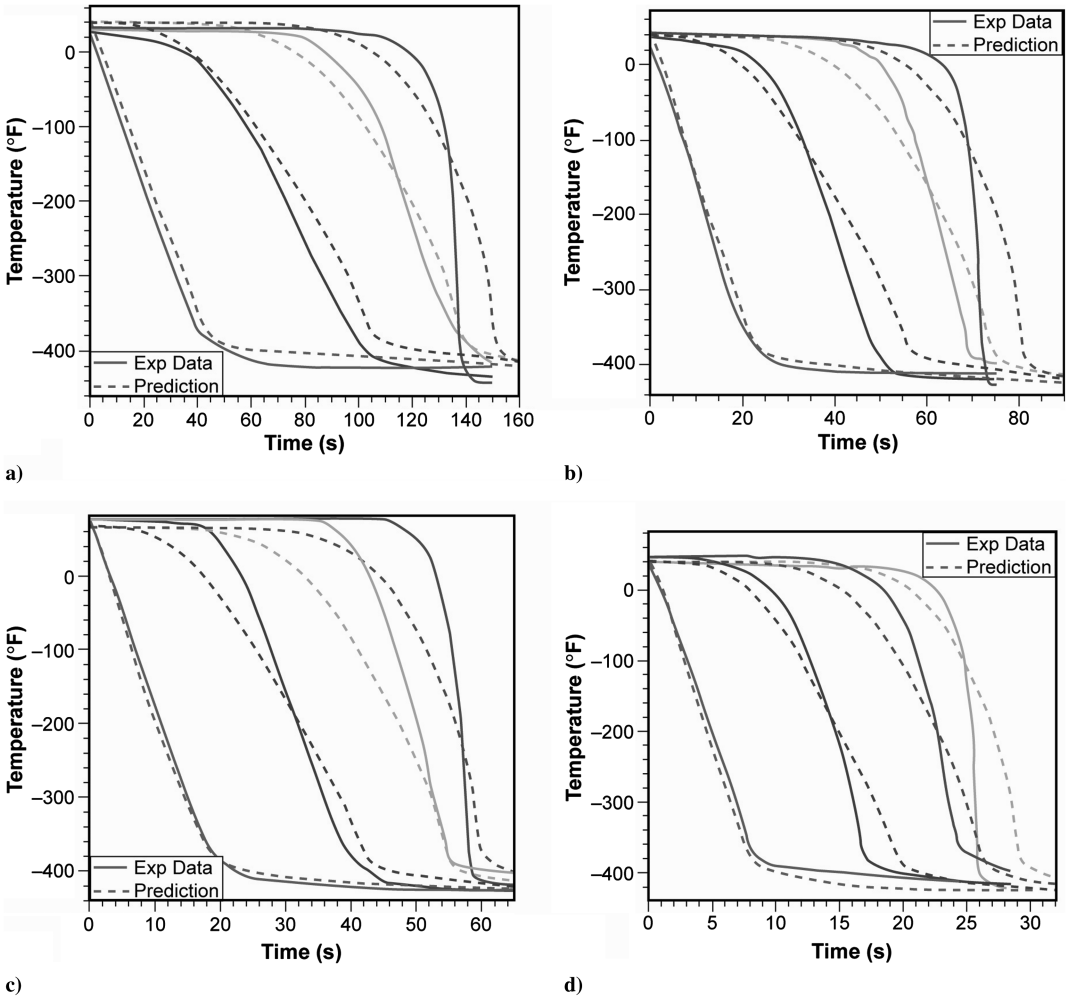

Fig. 5 Comparison of temperature histories for subcooled LH_2 for various driving pressures p: a) 36.74 psia, b) 61.72 psia, c) 86.7 psia, and d) 161 psia at four longitudinal stations: station 1 20 ft from the tank inlet, station 2 80 ft from the tank inlet, station 3 141 ft from the tank inlet, and station 4 198 ft from the tank inlet.

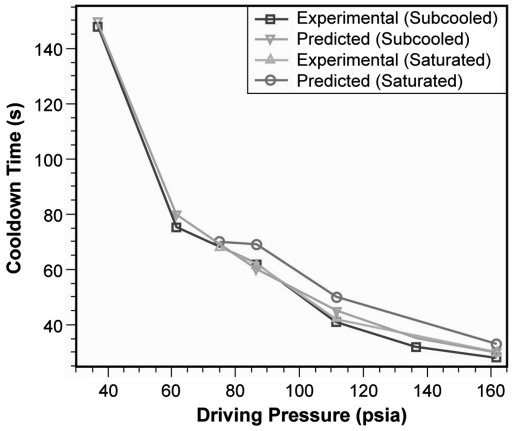

a)

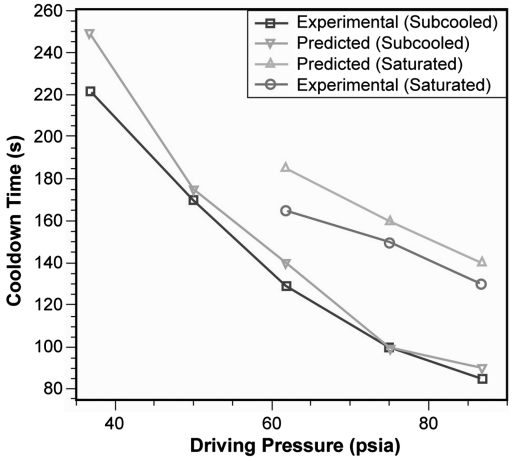

b)

Fig. 6 Subcooled and saturated liquid cryogen chilldown times: numerical predictions are compared with experiments for a) LH_2 and b) LN_2.

The effect of subcooling at the inlet liquid on chilldown time was marginal in the case of LH_2, which agrees with similar observations made in the experimental work. Our numerical experiments not reported here show that the accuracy of the prediction improves with an increase in the number of nodes in the model. chilldown time decreases with the increase in the driving pressure and thereby reduces the liquid consumption, as can be seen in Fig. 6a. This is to be expected since the higher driving pressure produces higher mass flux that, in turn, yields higher heat transfer coefficients. Subcooling the propellant in the tank reduces the chilldown time in general for all the cases studied.

Figure 7 shows a typical temperature history for the subcooled and saturated LH_2 at station 4. In the subcooled case, liquid cryogen chills down faster, due to a higher heat transfer coefficient in the subcooled case. Figure 8b shows the typical vapor quality for the subcooled and saturated cases for LH_2 at a station near the exit. It

Table 2 Subcooled (−424.57 °F) LH_2 chilldown time for various driving pressures

Driving pressure, psia	Experimental chilldown time, s	Predicted chilldown time, s
36.75	148	150
61.74	75	80
86.73	62	60
111.72	41	45
136.72	32	35
161.7	28	30

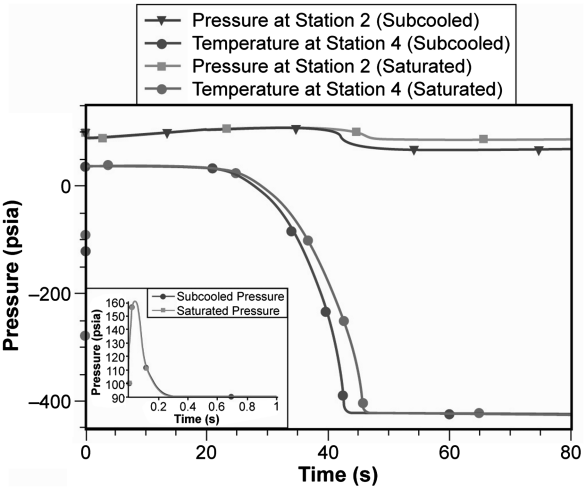

Fig. 7 Temperature (at station 4) and pressure (at station 2) history comparison between subcooled and saturated LH_2 for the driving pressure of 111.71 psia.

further confirms the chilldown behavior of these two cases. It shows that as the liquid front reaches the station, the vapor quality begins to drop and reaches a zero or near-zero value as the liquid front passes the station. It further shows that the quality reaches a perfect zero in the subcooled case.

Figure 9 shows the pressure history near the entrance (node 2) for the saturated and subcooled LH_2 for the driving pressure of

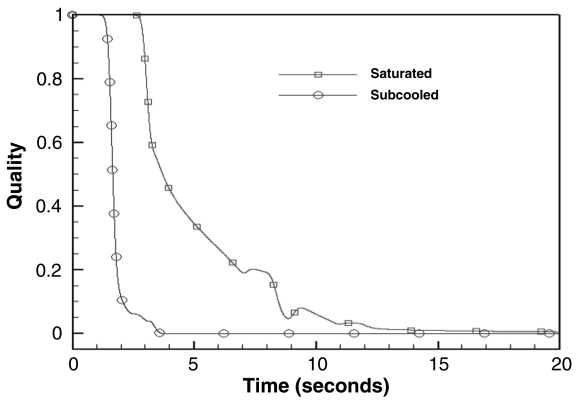

a)

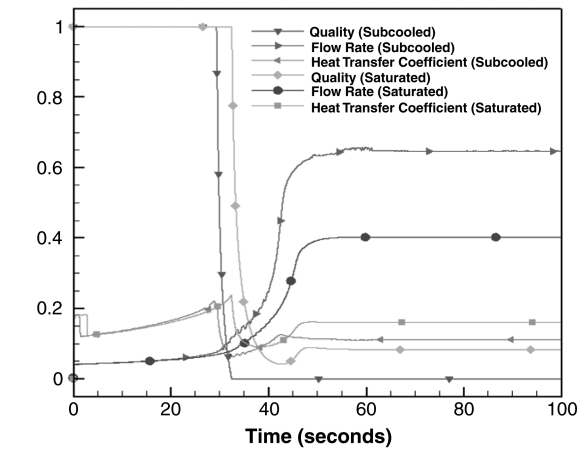

b)

Fig. 8 Plots comparing a) quality and history between subcooled and saturated LH_2 near the entrance of the pipe (node 2) for the driving pressure of 111.71 psia and b) quality, heat transfer coefficient, and flow rate for subcooled and saturated cases for the same driving pressure at station 2.

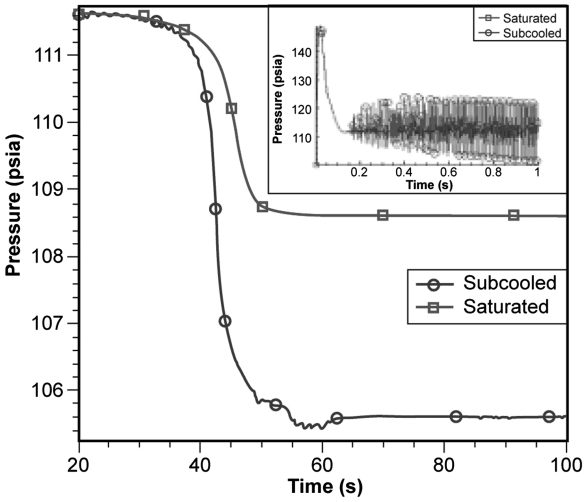

Fig. 9 Pressure-history comparison between subcooled and saturated LH_2 near the entrance of the pipe (node 2) for the driving pressure of 111.71 psia. Also shown in the inset is the initial pressure for the first 1 s.

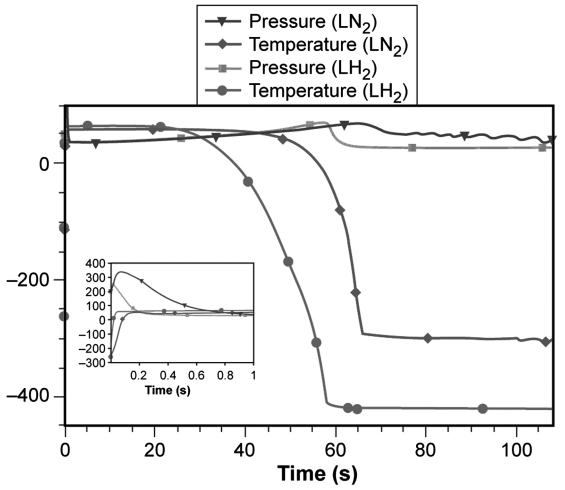

Fig. 10 Comparison of pressure and temperature between subcooled LH_2 and LN_2 at station 3 for the driving pressure of 86.7 psia.

111.71 psia. The pressure initially surges, exceeding the driving pressures, and subsequently oscillates for a few more seconds before stabilizing (see the inset in Fig. 9). These initial oscillations near the entrance (node 2 in the network model) of the pipe were typical in all cases and occurred only on nodes near the entrance. Oscillations typically last a few seconds and the oscillation is around the driving pressure level. As the flow moves away from the entrance, these oscillations begin to diminish. However, these peak (local maxima) pressures in the first few seconds, as well as the one that occurred immediately after condensation, occurred near the center of the pipeline, around station 2. These initial pressure surges were generally proportional to the driving pressure and reduced to levels below the driving pressure after a few seconds of the valve opening. Pressure surges subsequently increase to another peak, albeit smaller, proportional to the driving pressure, as the liquid front approaches the station (see Figs. 7 and 10).

The pressure subsequently drops to steady-state levels once the transfer line is condensed. However, the initial pressure peaks and oscillations are suppressed in the saturated case more so than in the subcooled case. One reason for not having oscillations in the saturated case is the presence of vapor that damps the oscillation. This can be seen in Fig. 8a, which shows quality-history comparison between subcooled and saturated LH_2 near the entrance of the pipe (node 2) for the driving pressure 111.71 psia. Figure 8b compares quality, flow rate, and heat transfer coefficient for subcooled and saturated LH_2 cases for the same driving pressure at station 2. As can be seen in the figure, the flow rate reaches higher steady-state values for the subcooled case than in the saturated case. It can also be seen that quality does not reach zero in the saturated case at the end of the simulation. This is one reason why the flow rate reaches higher steady-state values for the subcooled case.

Table 3 Saturated LN_2 chilldown time for various driving pressures

Driving pressure, psia	Saturation temperature, °F	Experimental chilldown time, s	Predicted chilldown time, s
61.74	−294.09	165	185
74.97	−289.71	150	160
86.73	−286.24	130	140

Table 4 Subcooled (−322.87 °F) LN_2 chilldown time for various driving pressures

Driving pressure, psia	Experimental chilldown time, s	Predicted chilldown TIME, s
36.75	222	250
49.97	170	175
61.74	129	140
74.79	100	100
86.73	85	90

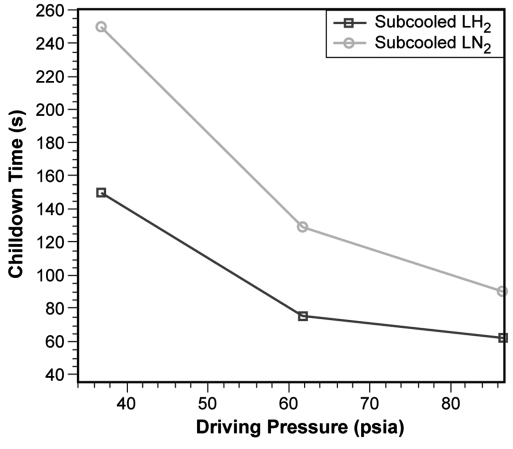

a)

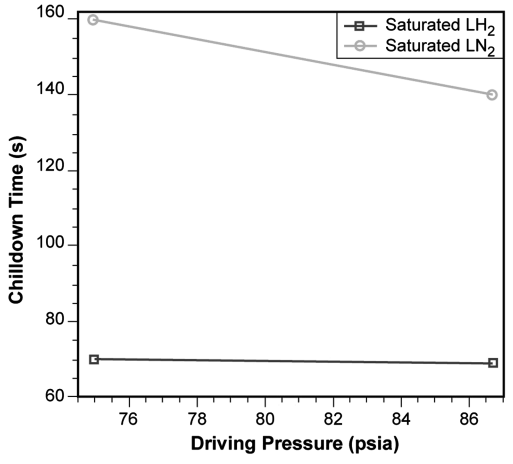

b)

Fig. 11 Effects of driving pressure on chilldown time are compared for LH_2 and LN_2: a) subcooled and b) saturated.

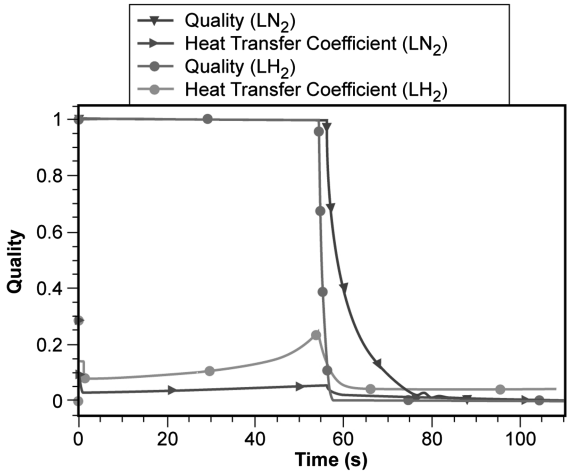

Fig. 12 Quality and heat transfer coefficient history of subcooled LH_2 and LN_2 for the driving pressure of 86.73 psia at station 3.

Mass flow rate increases as the liquid begins to propagate through the line and reaches steady state as the liquid fills the pipeline. The increase in flow rate and the steady-state values reached in the subcooled cases are, in general, higher than in the saturated cases. For LH_2, the mass flow rate increases by a factor of $\approx$10 in the saturated cases and by a factor of $\approx$15 to $\approx$20 in the subcooled cases. This is again due to the existence of vapor in the saturated cases. The heat transfer coefficient is higher when the cryogen is vapor than when it is liquid. The heat transfer coefficient increases with time until cryogen condenses; then it begins to decrease. This process is associated with a peak heat transfer coefficient value and this value increases with horizontal distance x. However, the values of the heat transfer coefficient in the fully vapor and fully liquid phases decrease with horizontal distance. It may also be noted from Fig. 9 that pressure at node 2 remains higher for the saturated case than for the subcooled case. This is because quality never reaches zero (Fig. 8) for the saturated case; as a result, the pressure does not go below saturation pressure.

B. Chilldown of Nitrogen

For the subcooled LN_2 cases, propellant temperature in the tank was $-322.87\,^{\circ}$F and pressure was varied to get different levels of subcooling. Whereas, for the saturated cases, the propellant temperature in the tank was the saturation temperature at the indicated driving pressure listed in Table 3. Figure 6b shows chilldown time as a function of driving pressure; see Tables 3 and 4 for the numerical values for the chilldown time and the corresponding driving pressure. As can be seen, subcooling had a significant effect on the chilldown time of nitrogen, as opposed to hydrogen, for which it had a marginal effect. Similar observations were reported in the experimental investigation reported in [9]. However, the initial pressure peak, especially near the entrance of the transfer line, is higher in the subcooled case than in the saturated case.

Flow rates also reach higher steady-state values in the subcooled case than in the saturated case. Vapor quality reaches a perfect zero in

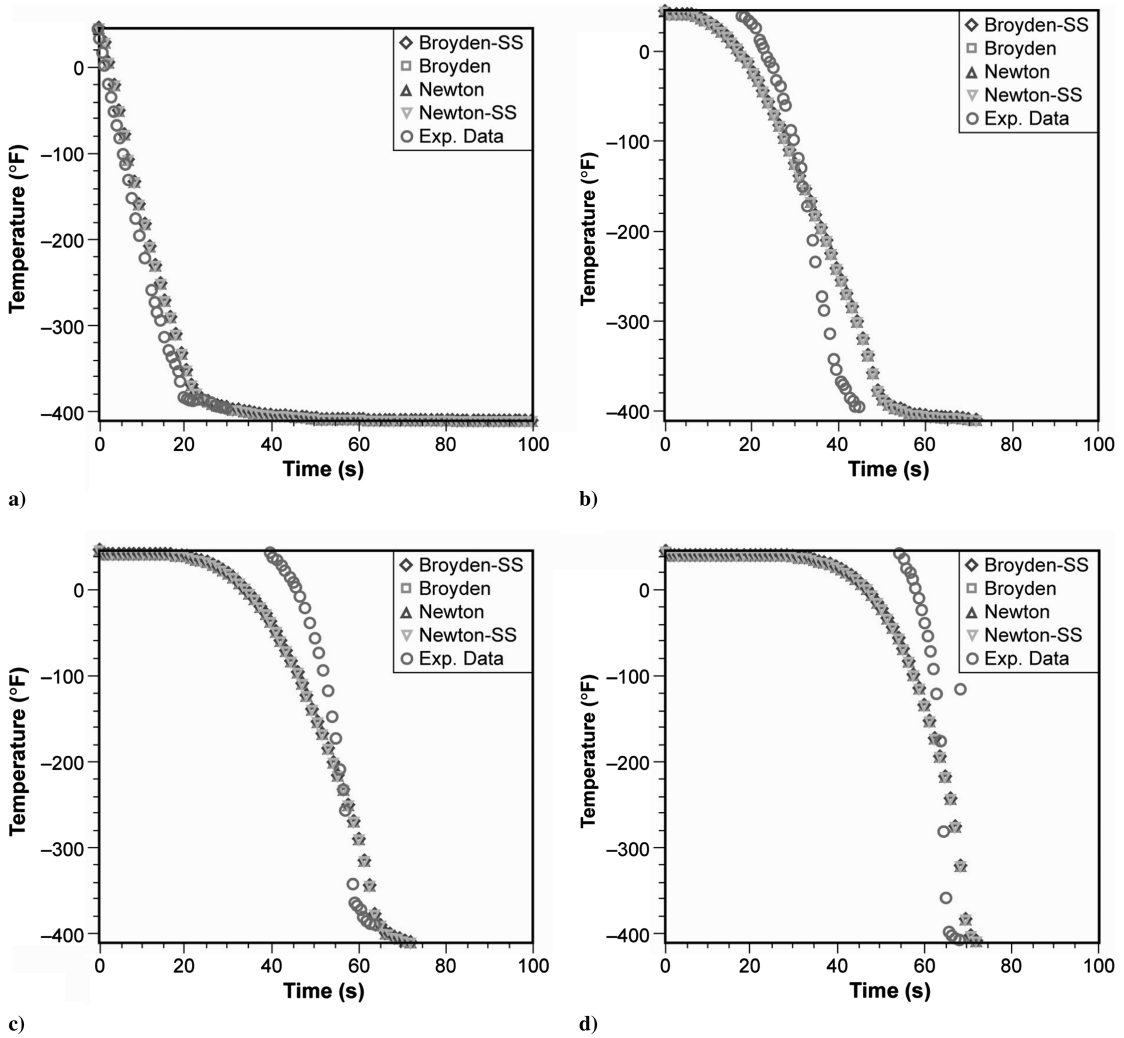

Fig. 13 Tube-wall temperature-history comparison of saturated LH_2 simulation with the four solvers for the driving pressure of 74.96 psia: a) station 1, b) station 2, c) station 3, and d) station 4.

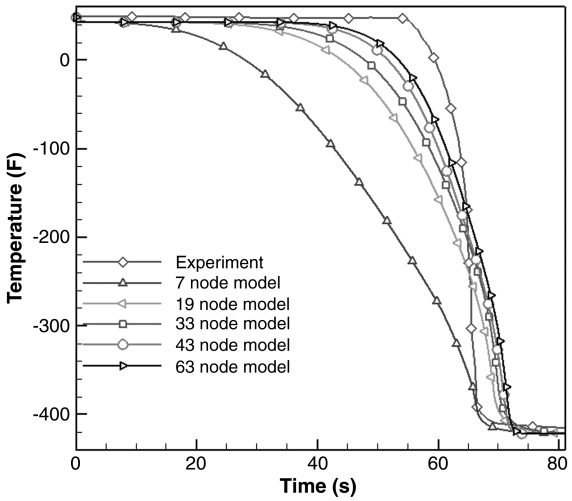

Fig. 14 Tube-wall temperature-history comparison of saturated LH_2 simulation with the five different grid models for the driving pressure of 74.96 psia at station 4.

the subcooled case; whereas in the saturated case, it does not. Also, chilldown time of LN_2 has a greater dependence on driving pressure than that of LH_2. This can be gleaned from the steepness of the LN_2 curve and LH_2 curve in Fig. 11.

In general, LN_2 takes longer to chill down than LH_2 (see Fig. 6b and Tables 1–4). This was true in all of the different driving pressures that may be attributed to the heat transfer coefficient being generally higher with hydrogen (see Fig. 12). Initial pressure surges are higher with nitrogen than with hydrogen in both the subcooled and saturated cases. A study of Fig. 6b shows that the predicted and experimental chilldown curves show better agreement at higher driving pressure levels. The numerical model overpredicts chilldown time more with nitrogen than with hydrogen, which may be attributed to the heat transfer correlation.

The models' predictions are in better agreement with the experiment in the subcooled cases than the saturated cases, in general, for both LH_2 and LN_2 (see Tables 1 and 2 and Fig. 6). The absence of nucleate boiling correlation in the model is a likely cause of the observed discrepancy. Mass flow rate increases as the LN_2 begins to propagate through the line and reaches steady state as the liquid fills the pipeline. The increase in flow rate and the steady-state values reached in the subcooled cases are, in general, higher than in the saturated cases. For LN_2, the mass flow rate increases by a factor of $\approx$6 in the saturated cases and by a factor of $\approx$12 in the subcooled cases. This is again due to the existence of vapor in the saturated cases. Although the factor of increase in mass flow rates in LN_2 is lower than that in LH_2, mass flow rate is generally higher in LN_2. However, the heat transfer coefficient of LH_2 is higher than that of LN_2 (see Fig. 12). This explains why the chilldown time of LH_2 is smaller than that of LN_2 (see Fig. 6 and Tables 1–4). Figure 10 shows the comparison of pressure and temperature at station 3 for subcooled LH_2 and LN_2 for the driving pressure of 86.7 psia. As can be seen, LH_2 chills down the line faster than LN_2, although the subcooled LH_2 temperature (−424.57 °F) was lower than the subcooled LN_2 temperature (−322.87 °F). This is because the heat transfer coefficient for LH_2 is higher than that for LN_2 (see Fig. 10). Increased heat transfer with LH_2, compared with LN_2, is additionally attributable to the facts that 1) $\rho_{vapor}/\rho_{liquid}$ for LN_2 is much greater than that of LH_2 and 2) latent heat of vaporization is greater for LH_2 than it is for LN_2. As a result, vapor formation may generate more backpressure in a LN_2 flow than in a LH_2 flow, thus reducing the velocity of the LN_2 flow.

Table 5 CPU time comparison with various solvers used to solve the conjugate heat transfer models[a]

Solver	CPU time, s
Newton-SS	12,571
Broyden-SS	6,403
Newton	19,006
Broyden	10,624

[a]Tolerance of 10^{-4}, $\Delta t = 0.0017$ s, and saturated LH_2 simulation for the driving pressure of 74.96 psia.

Figure 13 compares the transfer-line wall temperature of the 33-node transfer-line grid resolution predictions of the network model for saturated LH_2 simulation with the four solvers for the driving pressure of 74.96 psia. It also compares the predictions with the experimental transfer-line wall temperatures reported in [9]. By comparing the four cases in Fig. 13, it can be seen that the network models' predictions agree well with that reported in [9]. Our computational experiments with four different nonlinear solvers for conjugate heat transfer predictions discussed in this paper indicate that among the four solvers described in Sec. III, the Broyden-SS solver takes the least amount of computational time without losing accuracy. A Dell Precision T7400 computer with Intel Xeon, CPU 3.16 GHz with 16 GB RAM was used. Table 5 presents the CPU time taken by the four nonlinear solvers when used to solve the saturated LH_2 conjugate heat transfer problem for the driving pressure of 74.96 psia. Convergence was established when residuals were reduced to a value of 10^{-4} with the time-step size of 0.0017 s. However, all four solvers predict the solutions with the same accuracy in all the chilldown test cases reported in this paper. Figure 14 shows the results from grid refinement study. It clearly shows that the grid we used was fine enough to capture the essential physics.

IV. Conclusions

A fluid–solid coupled modeling implementation for conjugate heat transfer in flow network was presented. In this framework, conservation equations for both solid and fluids were solved simultaneously using an unsteady finite volume approach. The ability to accurately predict fluid and thermal transients was demonstrated by solving the strongly coupled fluid–solid-heat transfer problem of chilldown of a cryogenic transfer line. Test cases modeling transient flow of LH_2 and LN_2 under saturated and subcooled conditions were presented. The effects of varying the inlet driving pressure on the chilldown time and flow rates were evaluated. Increasing the driving pressure decreased the chilldown time and increased the flow rate.

Subcooling the inlet cryogen further reduced the chilldown time. This was more significant with LN_2 than with LH_2. Pressure and flow surges were generally higher with nitrogen. Moreover, nitrogen takes longer to chill down than does hydrogen. This can be attributed to the heat transfer coefficient being generally higher with hydrogen. chilldown of LN_2 had greater dependence on driving pressure than LH_2. The efficacy of the proposed approach was assessed by comparing the model predictions with experimentally measured wall temperature in several downstream positions in the transfer line. The numerical predictions matched well with measured results. The proposed model captured the essential features of conjugate heat transfer and provided an efficient and robust way for predicting chilldown of the transfer line at a low computational cost. Improved heat transfer coefficient correlation should further increase the accuracy of the model predictions.

Acknowledgments

This work was supported by a fellowship awarded to coauthor S. S. Ravindran under the NASA Summer Faculty program. S. S. Ravindran was also supported in part by NASA grant NNM05 AA22A with Melissa Van Dyke as Technical Contract Monitor. The work was conducted at NASA Marshall Space Flight Center, Huntsville, Alabama, in the ER43/Thermal Analysis Branch. The authors would like to thank the Thermal Analysis Branch for their support.

References

[1] Burke, J. C., Byrnes, W. R., Post, A. H., and Ruccia, F. E., "Pressurized Cooldown of Cryogenic Transfer Lines," *Advances in Cryogenic Engineering*, Vol. 4, 1960, pp. 378–394.

[2] Majumdar, A. K., and Ravindran, S. S., "Fast, Nonlinear Network Flow Solvers for Fluid and Thermal Transient Analysis," *International Journal of Numerical Methods for Heat & Fluid Flow*, Vol. 20, No. 6, 2010, pp. 617–637. doi:10.1108/09615531011056791

[3] Bronson, J. C., Edeskuty, F. J., Fretwell, J. H., Hammel, E. F., Keller, W. E., Meier, K. L., et al., "Problems in Cooldown of Cryogenic Systems," *Advances in Cryogenic Engineering*, Vol. 7, 1962, pp. 198–205.

[4] Antar, B. N., and Collins, F. G., "Flow Boiling During Quenching in Low Gravity Environment," *Microgravity Science and Technology*, Vol. 3, 1997, pp. 118–128.

[5] Cross, M. F., Majumdar, A. K., Bennett, J. C. Jr., and Malla, R. B., "Modeling of Chill Down in Cryogenic Transfer Lines," *Journal of Spacecraft and Rockets*, Vol. 39, No. 2, 2002, pp. 284–289. doi:10.2514/2.3810

[6] Chi, J. W. H., "Cooldown Temperatures and Cooldown Time During Mist Flow," *Advances in Cryogenic Engineering*, Vol. 10, 1965, pp. 330–340.

[7] Steward, W. G., Smith, R. V., and Brennan, J. A., "Cooldown Transients in Cryogenic Transfer Lines," *Advances in Cryogenic Engineering*, Vol. 15, 1970, pp. 354–363.

[8] Majumdar, A. K., and Steadman, T., "Numerical Modeling of Thermofluid Transients During Chilldown of Cryogenic Transfer Lines," 2003 SAE Conf., Society of Automotive Engineers, Paper 2003-01-2662, 2003.

[9] Brennan, J. A., Brentari, E. G., Smith, R. V., and Steward, W. G., "Cooldown of Cryogenic Transfer Lines—An Experimental Report," National Bureau of Standards, Rept. 9264, Nov. 1966.

[10] Van Dresar, N. T., Siegwarth, J. D., and Hasan, M. M., "Convective Heat Transfer Coefficients for Near-Horizontal Two-Phase Flow of Nitrogen and Hydrogen at Low Mass and Heat Flux," *Cryogenics*, Vol. 41, 2001, pp. 805–811. doi:10.1016/S0011-2275(01)00173-4

[11] Yuan, K., Ji, Y., and Chung, J. N., "Cryogenic Chilldown Process Under Low Flow Rates," *International Journal of Heat and Mass Transfer*, Vol. 50, Nos. 19–20, 2007, pp. 4011–4022. doi:10.1016/j.ijheatmasstransfer.2007.01.034

[12] Kawaji, M., Ng, Y. S., Banerjee, S., and Yadigaroglu, G., "Reflooding with Steady and Oscillatory Injection: Part I—Flow Regimes, Void Fraction, and Heat Transfer," *Journal of Heat Transfer*, Vol. 107, No. 3, 1985, pp. 670–678. doi:10.1115/1.3247476

[13] Majumdar, A. K., "Method and Apparatus for Predicting Unsteady Pressure and Flow Rate Distribution in a Fluid Network," U.S. Patent No. 7,542,885 B1, 2 June 2009.

[14] Patankar, S. V., *Numerical Heat Transfer and Fluid Flow*, Hemisphere, Washington, D.C., 1980.

[15] Colebrook, C. F., "Turbulent Flow in Pipes, with Particular Reference to the Transition Region Between Smooth and Rough Pipe Laws," *Journal of the Institution of Civil Engineers*, Vol. 11, 1939, pp. 133–156.

[16] Hendricks, R. C., Baron, A. K., and Peller, I. C., "GASP—A Computer Code for Calculating the Thermodynamic and Transport Properties for Ten Fluids: Parahydrogen, Helium, Neon, Methane, Nitrogen, Carbon Monoxide, Oxygen, Fluorine, Argon, and Carbon Dioxide," NASA Lewis Research Center TN D-7808, Cleveland, OH, Feb. 1975.

[17] Miropolski, Z. L., "Heat Transfer in Film Boiling of a Steam-Water Mixture in Steam Generating Tubes," *Teploenergetika*, Vol. 10, No. 5, 1963, pp. 49–52.

[18] Majumdar, A. K., "A Second Law Based Unstructured Finite Volume Procedure for Generalized Flow Simulation," AIAA Paper 99-0934, Aug. 1999.

[19] Majumdar, A. K., and Steadman, T., "Numerical Modeling of Pressurization of a Propellant Tank," *Journal of Propulsion and Power*, Vol. 17, No. 2, 2001, pp. 385–390. doi:10.2514/2.5754

[20] Broyden, C. G., "A Class of Methods for Solving Nonlinear Simultaneous Equations," *Mathematics of Computation*, Vol. 19, 1965, pp. 577–593.

K. Frendi
Associate Editor